Available online at www.sciencedirect.com
ScienceDirect
Trans. Nonferrous Met. Soc. China 34(2024) 1496−1506
Transactions of Nonferrous Metals Society of China
www.tnmsc.cn

Cathodic inhibition mechanism of magnesium alloys by using iron-complex inhibitor

Jun-jie YANG[1,2*], Lin-qian WANG[3*], Carsten BLAWERT[3], Sviatlana V. LAMAKA[3], Christian FEILER[3], Mikhail L. ZHELUDKEVICH[3,4], Wei LI[1]

1. Institute of Advanced Wear & Corrosion Resistant and Functional Materials, Jinan University, Guangzhou 510632, China;
2. Shaoguan Research Institute of Jinan University, Shaoguan 512027, China;
3. Institute of Surface Science, Helmholtz-Zentrum Hereon (Hereon), Geesthacht 21502, Germany;
4. Faculty of Engineering, University of Kiel, Kaiserstraße 2, Kiel 24143, Germany

Received 11 January 2023; accepted 19 September 2023

Abstract: The effect of a cathodic inhibitor (3-methylsalicylate, 3-MeSA) on the corrosion properties of Fe-contained pure Mg was investigated. The composition of Fe-rich particles, corrosion surface morphology, and molecular structure of 3-MeSA provide experimental and theoretical evidence for the corrosion behavior of Fe-contained Mg alloy and the corresponding cathodic inhibition mechanism of 3-MeSA. The results showed that silicon in a solid solution within Fe-rich particles was found, and the features of corrosion spots may correlate with different Fe/Si ratios. Although 3-MeSA can form an adsorptive layer on Mg substrate, its inhibition mechanism can be mainly ascribed to the capability to chelate Fe^{2+}/Fe^{3+} ions released from self-corrosion of Fe-rich particles, preventing the re-deposition of the reduced Fe species.

Key words: magnesium; iron-rich impurity; iron complex; cathodic inhibitor; quantum chemical calculation

1 Introduction

It is widely acknowledged that the corrosion of magnesium (Mg) can be significantly accelerated by transition metallic impurities, i.e., iron (Fe), cobalt (Co), copper (Cu) and nickel (Ni) since the equilibrium potential for Mg oxidation is lower than that of hydrogen evolution over a wide pH range (pH<11) [1−5]. As a result, impurities with low overpotential for hydrogen evolution promotes the corrosion of Mg substrates due to the increasing rate of hydrogen evolution [6,7]. Among the known impurities, Fe is the most commonly encountered and deleterious element for Mg alloys because it is easily introduced throughout the whole production chain, e.g., from melting pots and stirring tools made of steel [8]. The tolerance limit of Fe in Mg (as-cast) has been reported to be in the range of $(170−180)\times10^{-6}$ (mass fraction), above which Fe precipitates and accelerates the corrosion rate significantly in the function of its content [9−12]. However, even much smaller amounts of Fe can be detrimental in the presence of Si, which promotes the nucleation and growth of Fe-rich particles in the Mg matrix [13]. The corrosion of Mg usually initializes from these Fe sites due to the formation of micro-galvanic coupling between Mg and Fe. Simultaneously, the corroded areas (nominally dark areas) expand either in the form of discs or filiform-tracks with increasing immersion time, and a transition from disc-form corrosion to filiform

* Jun-jie YANG and Lin-qian WANG contributed equally to this work
Corresponding author: Jun-jie YANG, Tel: +86-15547287612, E-mail: junjieyang0612@gmail.com
DOI: 10.1016/S1003-6326(24)66486-1

corrosion (FFC) can occur with decreasing Fe content or concentration of NaCl solution [14].

Up to date, the effect of Fe impurities on the corrosion of Mg is still of particular interest [15−18] since it can be adopted in explaining the negative difference effect (NDE) [15] and even the corrosion mechanism of Mg alloys [19]. However, the experimental validation of these assumptions is limited due to the 10^{-6} (mass fraction) level and micron size (0.3−3 μm [20]) of Fe impurities in Mg substrates, which are beyond the resolution of most typical characterization techniques to detect, especially after corrosion of Fe-containing Mg substrates [6,21]. For this reason, a series of novel higher-resolution characterization techniques were adopted to study the evolution of Fe-rich particles during the corrosion process of Mg substrates. For instance, transmission electron microscopy (TEM) was employed by TAHERI et al [21], who disclosed that a Fe-rich particle detached from the Mg substrate embedded within the outer column mixed $Mg(OH)_2$−MgO layer, which might catalyze the local cathodic process (or hydrogen evolution reaction, HER). High-resolution Rutherford back-scattering spectrometry (RBS) was used by CAIN et al [6] to examine the elemental composition of the corrosion layer as a function of its depth. With the combination of RBS and inductively coupled plasma atomic emission spectroscopy (ICP−OES) results, they confirmed the Fe enrichment on the corroded Mg surface based on direct examination and mass balance considerations. To have a mechanistic understanding of the evolution of Fe impurities during the corrosion of Mg substrate, HÖCHE et al [22] and YASAKAU et al [23] performed a study by introducing magnetic field and versatile surface characterization techniques. They suggest that Fe-rich particles trigger the anodic dissolution of surrounded Mg, then gradually detach from the Mg substrate due to the undermining effect or probable release of H_2. As a result, the dissolved Fe is oxidized to Fe^{2+}/Fe^{3+} or Fe_2O_3 species, which re-deposit onto the Mg surface, especially at the corrosion front, through both chemical and electrochemical reduction reactions. Most recently, significant segregation of Fe impurity at grain boundaries has been observed on corroded Mg surfaces by employing 3D time-of-flight secondary ion mass spectrometry (ToF-SIMS) by MERCIER et al [24]. In addition to Fe, such a re-deposition mechanism was also reported for other noble impurities (e.g., copper (Cu) and silver (Ag)) for Mg alloys [25,26].

Based on the Fe re-deposition mechanism, a novel concept for screening corrosion inhibitors was developed by LAMAKA et al [27], in which the complex formation ability between inhibitor anions and Fe^{2+}/Fe^{3+} is seen as a critical factor in determining the effect of potential inhibitors. They correlated the relationship between the inhibition efficiency and complex forming capability for five different inhibitors (i.e., cyanide, salicylate, oxalate, 5-methylsalicylate and thiocyanate). This concept was further confirmed by testing 150 individual compounds for their ability to modulate the corrosion of six Mg alloys and three grades of pure Mg [28]. In this work, 3-methylsalicylate (3-MeSA) was identified as one of the most efficient and environmentally benign corrosion inhibitors for CP-Mg, RE- and Al-containing Mg alloys. The superior corrosion inhibition performance of this cathodic inhibitor was further studied in our previous work by employing a series of electro-chemical and surface characterization techniques (such as hydrogen evolution, electrochemical measurements, scanning Kelvin probe force microscopy (SKPFM), and ATR-FTIR in Kretschmann geometry integrated with EIS measurements [29,30]). Therein, the cathodic inhibition mechanism of 3-MeSA was described as follows: (1) blockage of H_2O reduction on Fe-rich particles due to the adsorption of 3-MeSA and/or due to the precipitation of denser $Mg(OH)_2$ layer; (2) complexation of Fe^{2+}/Fe^{3+} ions to suppress their re-deposition onto the Mg surface.

Although the Fe tolerance limit in Mg alloys was widely accepted, inconsistent results were reported by YANG et al [13,31], who observed a high corrosion rate for pure Mg only containing 25×10^{-6} Fe or 50×10^{-6} Fe. According to the simulated Mg−Fe−Si ternary phase diagram, they suggested that the presence of trace silicon (Si) favored the formation and growth of Fe-rich particles, which resulted in a higher corrosion rate of Mg-containing Fe impurities below its tolerance limit. In the present work, the inhibition mechanism of the cathodic corrosion inhibitor 3-MeSA was further investigated. The surface of Mg containing excessive Fe impurity (i.e., 342×10^{-6}) was analyzed by experimental and theoretical methods after a

corrosion test in NaCl electrolyte with inhibitor addition. The presented results not only unveiled the role of Si regarding Fe impurities but also provided further support to the Fe re-deposition mechanism and cathodic inhibition mechanism by Fe-complexing agents.

2 Experimental

2.1 Materials and reagents

As-cast pure Mg (99.94 wt.%) specimens with dimensions of 15 mm × 15 mm × 4 mm were used for corrosion tests. The contents of impurities were determined to be 342×10^{-6} Fe, 3×10^{-6} Cu, 207×10^{-6} Si and less than 2×10^{-6} Ni by Spark OES (Spark analyzer M9, Spectro Ametek, Germany). Prior to corrosion testing, all specimens were ground using emery papers up to 1200 grit, rinsed with deionized water and ethanol, and eventually dried in pressed air flow at room temperature. 3-methylsalicylic acid (3-MeSA, Sigma-Aldrich Chemie GmbH, Germany) was dissolved in 0.5 wt.% NaCl solution without any further purification, and standard NaOH solution (1 mol/L) was used to adjust the pH value of the solution until a neutral level (pH 6.8−7.2) was achieved. Deionized water served as a solvent for all the solutions in the present work.

2.2 Electrochemical measurements

A conventional three-electrode system with Gamry Interface 1000E potentiostat was used to record the open circuit potential (OCP) for Mg−342Fe (mass fraction, 10^{-6}) immersed in NaCl electrolytes without and with the addition of 3-MeSA. During the measurement, Mg coupons with 1 cm^2 exposed surface area served as the working electrode, a platinum wire as the counter electrode and a saturated Ag/AgCl as the reference electrode.

2.3 Morphology and composition characterization

A crossbeam workstation AURIGA 40 (Zeiss, Germany) equipped with a focused ion beam (FIB) column and scanning electron microscope (SEM) was used for preparing the cross-sections and observing the Fe-rich particles as well as characteristic regions on the corroded surface. EDAX (Ametek GmbH, Wiesbaden, Germany) was used for the composition analysis. A Philips CM200 transmission electron microscopy (TEM) operated at 200 kV and an FEI Titan 80-300 TEM with a Cs image corrector operated at 300 kV were used to identify the structure of Fe-rich particles. Elemental analysis was performed using X-ray energy dispersive spectroscopy (EDS) in scanning TEM (STEM) mode.

2.4 Quantum chemical calculation

Geometrical optimization of deprotonated 3-MeSA was conducted using Gaussian 16 program package at the B3LYP/6-31+G** of level density functional theory (DFT). Effects of water solvation are included by using a self-consistent reaction field (SCRF) with a polarizable continuum model (PCM).

3 Results and discussion

3.1 Morphology and composition of Fe-rich impurities

The Fe-rich particles can be easily identified in the backscattered electron (BSE) mode since the content of Fe in Mg−342Fe is significantly higher than its tolerance limit to form precipitate according to the thermodynamic phase calculation [7,13]. The morphology of 20 individual Fe-rich particles with Fe/Si mass ratio of 1.9−18.4 observed from the well-polished Mg−342Fe surface is illustrated in Fig. S1 (Supporting Information). Most of the Fe-rich particles are cuboid-shaped and the length of edges ranges from 290 to 570 nm. As reported in our previous work [29] and Refs. [7,13], Si is a detectable mass element in Fe-rich particles. However, the Fe/Si mass ratio varies in a relatively wide range (2.7−16).

Figure 1 shows the TEM and EDS analysis results of the Fe-rich particles in the Mg−342Fe substrate. By tilting the specimens, selected-area diffraction patterns were taken from different zones for both Fe-rich particles and the Mg matrix. By analyzing the diffraction patterns and comparing them with the simulated ones shown in Fig. 1(b), these Fe-rich particles are identified as body-centered cubic (bcc) α-Fe phase with a space group of $Im\bar{3}m$. The lattice parameter is around 0.28 nm. EDS analysis results in Fig. 1(c) further confirm the existence of Si in the particles and reveals a Fe/Si mass ratio in a range of 3−7. The TEM investigation in this study confirms the prediction in literature [13] that these Fe-rich particles have a

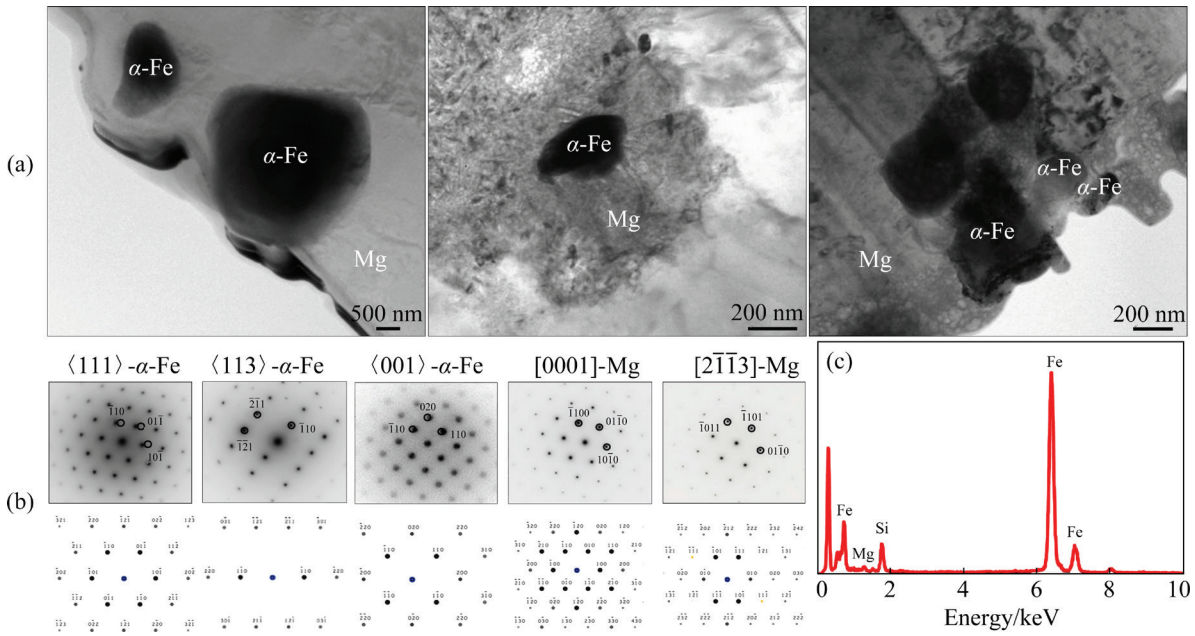

Fig. 1 TEM and EDS analysis results of Fe-rich particles in commercially pure Mg−342Fe: (a) Bright-filed TEM images; (b) Experimental and simulated diffraction patterns from ⟨111⟩, ⟨113⟩ and ⟨001⟩ zone axes of Fe-rich particles and [0001] and [2$\bar{1}\bar{1}$3] orientations of Mg matrix; (c) EDS analysis results of Fe-rich particles

bcc structure and that Si atoms are in solid solution state in the α-Fe phase.

3.2 Electrochemical performance

Without external polarization, the free corrosion properties of the working electrode (specimen) can be obtained from OCP data. Figure 2 presents the variation of OCP as a function of time for Mg−342Fe immersed in blank NaCl solution with the addition of 0.05 mol/L 3-MeSA directly at the beginning and after 300 s, respectively. As a reference, a high purity Mg containing 54×10^{-6} Fe (mass fraction) (Mg−54Fe with Ni less than 2.0×10^{-6}, 3.6×10^{-6} Cu and 207×10^{-6} Si) was also measured. Figure 2 shows a less noble OCP value at the beginning of immersion, which shortly (after 100 s immersion) stabilizes at around −1.80 V in inhibitor-free NaCl solution. This typical potential response may be ascribed to the formation of a $MgO/Mg(OH)_2$ layer on the Mg surface, which balances the Mg oxidation (anodic) and hydrogen evolution (cathodic) reaction in the corrosion cell. Mg−342Fe, containing sixfold of the tolerance limit of Fe in Mg, shows a similar trend of OCP, increasing from −1.82 V (0 s) to −1.72 V (100 s). Since then, the consecutive positive shift of OCP is sustained at a slightly moderate rate,

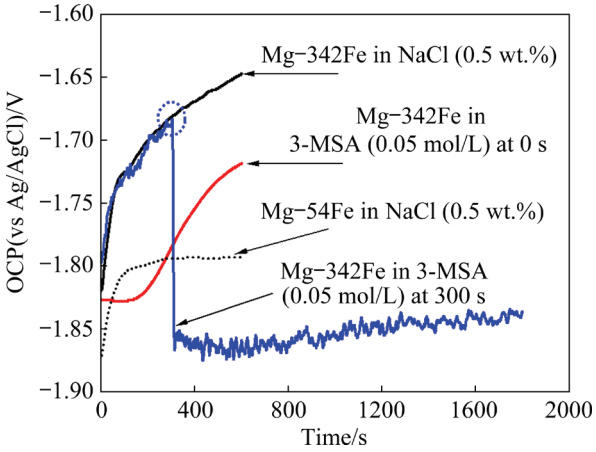

Fig. 2 Variation of OCP as function of time for Mg−54Fe (reference) and Mg−342Fe immersed in blank NaCl solution without and with addition of 3-MeSA after 0 and 300 s stabilization

indicating the continuous corrosion of Mg due to only the partially protective nature of hydroxide film influenced by the Fe-rich inclusions [31]. Immersing the Mg−342Fe into the NaCl solution containing 0.05 mol/L 3-MeSA shifts the whole OCP curve uniformly towards the negative potential direction, which indicates the suppression of hydrogen evolution in the corrosion cell [32].

Considering cathodic inhibition mechanism proposed by LAMAKA et al [27], the complex

formation constant for 3-MeSA chelating with Fe^{3+} is lg K=18.13 at 25 °C [33], which suggests that a high inhibition efficiency of 3-MeSA can be achieved through the complexation of Fe^{2+}/Fe^{3+} and inhibitor molecules by forming a soluble complex. YANG et al [29] validated the high inhibition efficiency of 3-MeSA through hydrogen evolution and electrochemical methods. The essence of this mechanism is the chelation of Fe^{2+}/Fe^{3+} ions which are a product of the self-corrosion of Fe-rich particles and subsequent prevention of their reduction and re-plating onto the Mg surface. Moreover, the suppression of Fe activity is also significantly influenced when the same amount of 3-MeSA is added into a blank NaCl solution after 300 s of immersion, as indicated by an instant drop of OCP from −1.67 to −1.85 V. This fast response of OCP can be otherwise ascribed to the physisorption of inhibitor molecules on Fe-rich particles, in which Fe-rich particles and inhibitor interact based on dipolar attraction, van der Waals forces or hydrogen bonding. As a result, both chemisorption and physisorption behaviors contribute to the corrosion reduction of Mg−342Fe. However, the weighting factor in the corrosion inhibition of chemisorption may be higher than that of physisorption since the physisorption is normally less stable and sensitive to several environment factors (e.g. temperature, pH and flow rate) [34].

3.3 Morphology and composition of corroded surface

The surface morphologies of Mg−342Fe immersed in 0.5 wt.% NaCl solution with the addition of 0.05 mol/L 3-MeSA for 24 h are shown in Fig. 3. It is easy to confirm the effectiveness of 3-MeSA by comparing the optical microscopy images of the samples immersed in solutions without and with inhibitor addition (Fig. 3(a)). The integrity of the surface is destroyed in the blank NaCl electrolyte, producing dark and loose corrosion products, whereas a relatively intact surface condition is found on the surface protected by 3-MeSA.

Performing a closer observation (Fig. 3(b)) of the inhibitor-protected specimen unveils three typical corrosion features, including saucer-like spots (Type A), ring-shape spots (Type B) and dormant spots (Type C). The diameters of A- and B-type corrosion spots are 20−40 μm, while the central cores (around 5 μm in diameter) in A-type spots are absent in B-type spots. Since Fe-rich particles are the only impurity inclusions in the used material, the central cores in A-type features

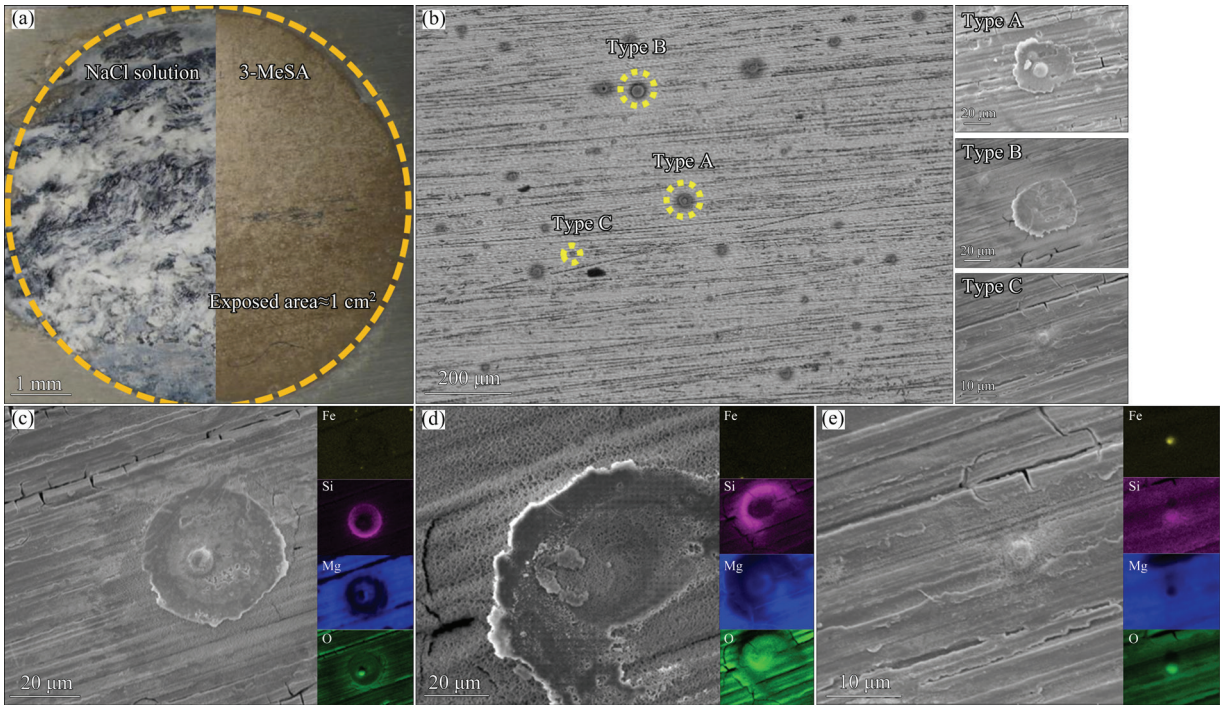

Fig. 3 Surface morphologies of Mg−342Fe immersed in 0.5 wt.% NaCl solution containing 0.05 mol/L 3-MeSA for 24 h: (a) OM image of exposed area (≈1 cm²); (b) SEM image of corroded area including saucer-like spot (Type A) (c), ring-shape spot (Type B) (d) and dormant Fe spot (Type C) (e)

highly indicate their locations. Both A- and B-type spots agree well with the radial corrosion propagation tendency observed for pure Mg with excessive Fe described in Refs. [14,31], and the presence or absence of the cores may suggest different evolution mechanisms for Fe-rich particles. On the other hand, the dimension of C-type corrosion features is much smaller (≈2 μm) compared to the former counterparts. More importantly, the existence of Fe is verified by EDS analysis (Fig. 3(e)), which is in good agreement with similar features on corroded pure Mg containing around 220×10^{-6} Fe [23]. Moreover, C-type Fe-containing spots reveal negligible corroded area compared to the other two types, and they can be considered as dormant Fe spots.

As assumed in Ref. [31] and experimentally supported by TAHERI et al [21], these C-type Fe particles may be an iron oxide (i.e., Fe_xO_y), which induce less active galvanic coupling with Mg substrates. In particular, it is of great interest to notice the homogenous distribution of Si, rather than Fe, along the periphery of A- and B-type spots, which suggests the self-corrosion of Fe-rich particles and subsequent chelating of these Fe species (e.g., Fe^{2+} and/or Fe^{3+}) with 3-MeSA. When Fe-rich particles are dissolved, coexisting Si gets liberated. Si-containing corrosion products (e.g., silicon hydroxide [35] and magnesium trisilicate ($2MgO\cdot3SiO_2\cdot xH_2O$) [36]) precipitate on Mg surface and serve as indicator for dissolution of Fe-rich particles.

To trace the Fe-rich particles and elucidate the results shown in EDS, each of the A- and B-type spots was milled by FIB from the perimeter towards the middle, and the cross-section of half-milled spots is presented in Fig. 4. Current (1−2 nA) was employed for the milling process to ensure that only a thin slice is removed in each cycle to prevent overlooking Fe particles. The single removal rate was 0.07 μm corresponding to 560 slices over the area of 1600 μm^2. The milling process of the remaining half B-type spot is provided as a video file in the Supporting Information. It is clear from the cross-section of both samples that corrosion product layers with an average thickness of less than 5 μm are shown on the surface of Mg. Moreover, a Fe-rich particle is detected under the middle core of the A-type corrosion spot situated at the interface between the Mg substrate and the corrosion product layer. In contrast, no particles are found within the B-type spot throughout the area (shown in the video of Supporting Information). The existence of the hidden Fe-rich particle, not

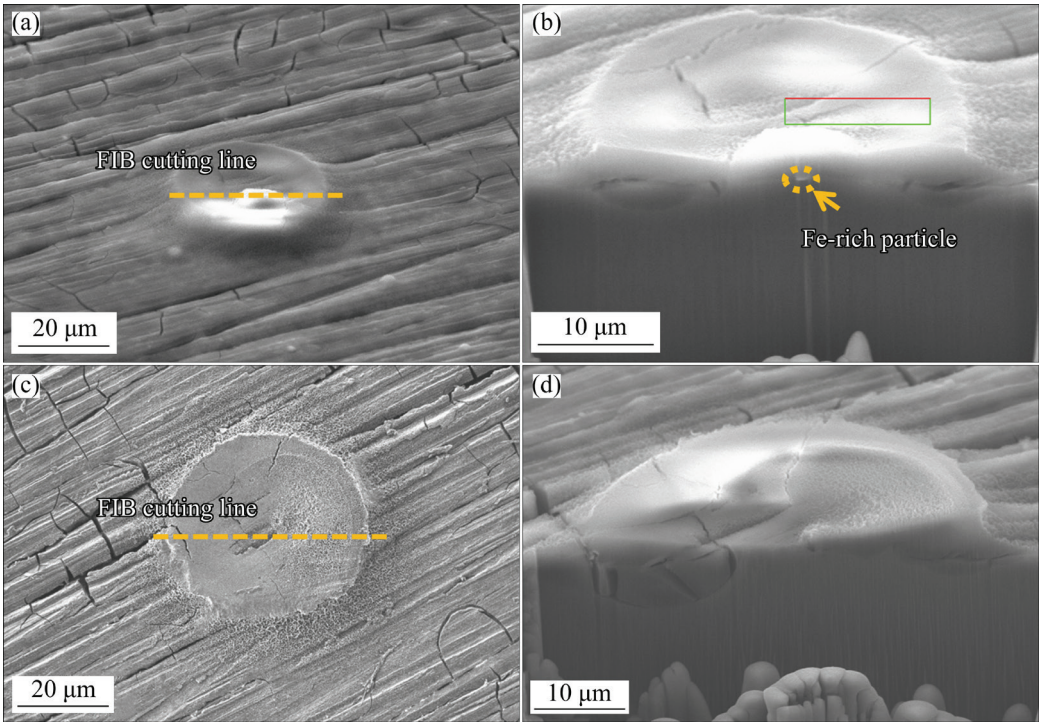

Fig. 4 Surface (a, c) and cross-section (with 15° tilt of sample plate) (b, d) morphologies of A- and B-type corrosion spots

revealed in EDS, can be ascribed to the greater thickness of the hydroxide layer that restricts X-ray penetration.

3.4 Molecular properties of 3-MeSA

Figure 5 shows the Mulliken charges of the atoms in the geometry-optimized molecule of deprotonated 3-MeSA and its frontier orbitals. Molecular properties that were derived from the DFT calculations (i.e., the highest occupied molecular orbital energy (E_{HOMO}), the lowest unoccupied molecular orbital energy (E_{LUMO}), energy gap ($\Delta E_{HL}=E_{LUMO}-E_{HOMO}$), electronegativity ($\chi$), global hardness ($\eta$) and the fraction of electrons transferred from inhibitor to metallic surface (ΔN)) are listed in Table 1. ΔN is determined depending on the quantum chemical equation [37,38]:

$$\Delta N=\frac{\chi_{Fe}-\chi_{Inh}}{2(\eta_{Fe}-\eta_{Inh})} \quad (1)$$

where $\chi_{Fe}=7$ [38,39], $\eta_{Fe}=0$ [38,39], $\chi_{Inh}=(I_{Inh}+Y_{Inh})/2$ [40] and $\eta_{Inh}=(I_{Inh}+Y_{Inh})/2$ [40], while the ionization potential $I_{Inh}=-E_{HOMO}$ [38] and electron affinity $Y_{Inh}=-E_{LUMO}$ [38]. As can be seen from Fig. 5(b), the highest negative charges are located on the O atoms with values of −0.734 (O1), −0.708 (O2) and −0.754 (O3), which represent the binding sites for the complexation of released Fe ions. E_{HOMO} is a parameter usually associated with the electron-donating ability of a molecule, and a higher E_{HOMO} value indicates a stronger tendency of the molecule to donate electrons towards the unoccupied orbital

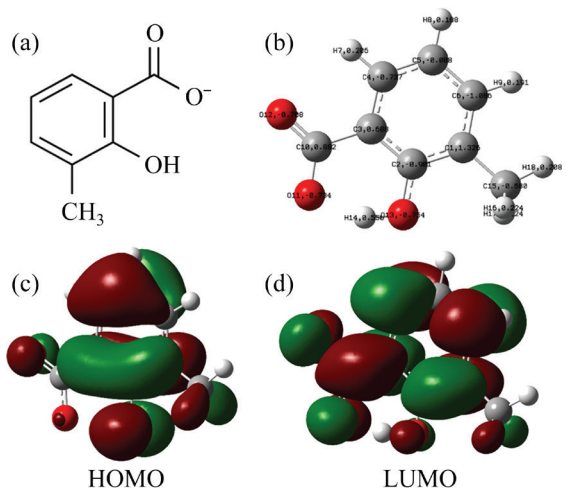

Fig. 5 Molecular formula (a), optimized molecular structure (b) and frontier molecule orbital density distributions (HOMO (c) and LUMO (d)) of deprotonated 3-MeSA

Table 1 Quantum chemical parameters of deprotonated 3-MeSA using DFT method

E_{HOMO}/eV	E_{LUMO}/eV	ΔE_{HL}/eV	χ	η	ΔN
−5.94	−0.78	5.15	3.361	2.577	0.705

of an acceptor with lower energy. Meanwhile, E_{LUMO} implies the ability to accept electrons; hence, a lower E_{LUMO} value indicates more possibility to accept electrons [41].

Steady adsorption of 3-MeSA on Fe-rich impurities is also not expected due to the consecutive release of hydrogen bubbles and their stabilization on the sample surface. As a result, Fe-rich particles gradually sink within the $Mg(OH)_2$ corrosion layer due to the dissolution of the Mg substrate and the galvanic coupling does not cease until the Fe-rich particles detach from the metallic substrate by undermining or being isolated by hydrogen bubbles [17,21,31]. After that, Fe^{n+} (n=2 and 3) ions are produced due to the chemical dissolution of isolated Fe-rich particles. A small frontier orbital energy gap indicates relatively high affinity to compounds like 3-MeSA concerning the complexation of the d-elements (e.g., Fe). Concomitantly, the correlation between ΔE_{HL} and inhibiting efficiencies has been recently reported by FEILER et al [42,43] for commercially pure Mg containing 220×10^{-6} Fe. They concluded that the correlation with the inhibiting efficiencies exists because of the unique re-plating mechanism that plays a key role in the corrosion process of commercially pure Mg. Furthermore, they demonstrated that the inhibition efficiencies for Mg−220Fe and Mg−342Fe agree well for compounds exhibiting an inhibiting effect. Hence, it is assumed that ΔE_{HL} can also be applied as an indicator for inhibition efficiencies of Mg−342Fe, even though the correlation of the frontier orbital energy gaps with inhibiting efficiencies for materials based on copper, aluminum or steel is essentially zero.

3.5 Corrosion inhibition mechanism of 3-MeSA

With the combination of the experimental and theoretical analysis results, the cathodic inhibition mechanism reported in our previous work [29] can be further confirmed, as shown in Fig. 6. When Mg−342Fe is immersed in the NaCl solution with addition of 3-MeSA, the reduction of corrosion reaction probably results from the physisorption and

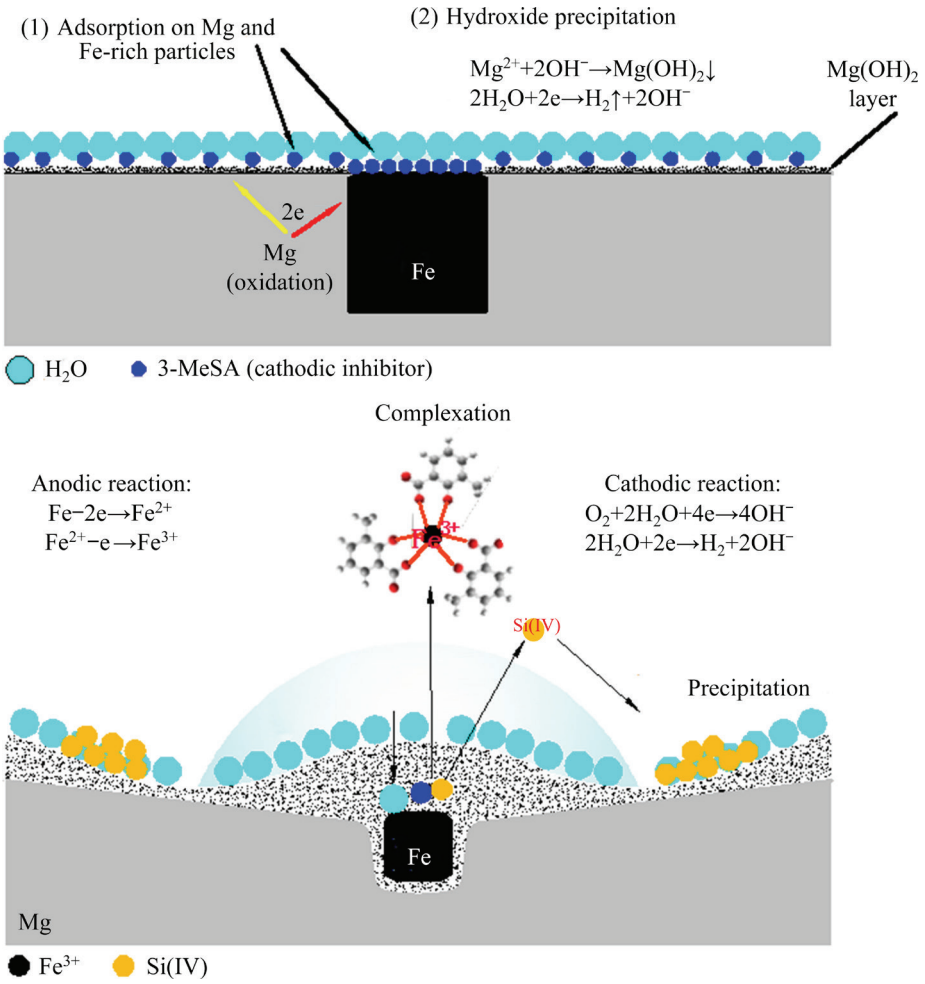

Fig. 6 Corrosion inhibition mechanism of Mg containing Fe impurities using deprotonated 3-MeSA as cathodic inhibitor

chemisorption of 3-MeSA anion on the surface of Fe-rich particles and Mg substrate. Both Mg oxidation (i.e., $Mg-2e\rightarrow Mg^{2+}$) and H_2O and O_2 reduction ($2H_2O+2e\rightarrow H_2+2OH^-$, $2H_2O+O_2+4e\rightarrow 4OH^-$) on Fe-rich particles are correspondingly inhibited. Simultaneously, precipitation of $Mg(OH)_2$ also contributes to the decrease of corrosion rate, as local pH rises to around 10.5 within the first minutes of immersion [44,45]. Subsequently, the dissolution of Fe-rich particles occurs due to their undermining, followed by detachment and self-corrosion (Anodic reaction: $Fe-2e\rightarrow Fe^{2+}$, $Fe^{2+}-e\rightarrow Fe^{3+}$; Cathodic reaction: $2H_2O+O_2+4e\rightarrow 4OH^-$). However, the self-corrosion behaviors of Fe-rich particles are closely related to their compositions. It seems to be much easier for the Fe particles containing a higher content of Si (A-type and B-type) to undergo self-corrosion compared to those smaller purer Fe particles (C-type) with higher Fe content. The re-deposition of the Fe^{2+}/Fe^{3+} cations upon the surface does not occur because Fe^{2+}/Fe^{3+} ions are bound by 3-MeSA forming soluble Fe−Inh complexes (lg K at 25 °C is 18.13 [33]). However, the behavior of released silicon species is less affected by 3-MeSA and most of them precipitate along the periphery of corrosion spots. Hydrogen bubbles also play an important role in affecting the self-corrosion behavior of Fe-rich particles and determining the subsequent distribution of Si. However, the influencing mechanism is still unclear at the current stage and is currently investigated in more detail.

4 Conclusions

(1) Due to the existence of an excessive amount (342×10^{-6}, mass fraction) of Fe impurities, the commercially pure Mg−342Fe reveals a significant tendency to suffer corrosion attack in NaCl solution. In addition to α-Fe, Si was identified

in a solid solution within the Fe-rich particles of Mg−342Fe. The precipitation of Si-rich corrosion products was found as circular features formed during the dissolution of Fe-rich particles. This finding provides additional evidence for the dissolution of Fe-rich particles during the corrosion of Mg.

(2) Three typical corrosion spots can be identified on the corroded surface protected by 3-MeSA, which may result from Fe-rich particles with different Fe/Si ratios.

(3) 3-MeSA can effectively inhibit the corrosion process of Mg−342Fe through adsorption on the surface of Fe-rich particles and its complexation ability with Fe^{2+}/Fe^{3+} that effectively reduces the re-deposition of Fe^{2+}/Fe^{3+} onto Mg surface.

CRediT authorship contribution statement

Jun-jie YANG: Investigation, Data curation, Visualization, Formal analysis, Validation, Writing − Original draft; **Lin-qian WANG:** Investigation, Formal analysis, Validation, Writing − Review & editing; **Carsten BLAWERT:** Supervision, Writing − Review & editing; **Sviatlana V. LAMAKA:** Supervision, Formal analysis, Investigation, Writing − Review & editing; **Christian FEILER:** Investigation, Data curation, Formal analysis, Writing − Review & editing; **Mikhail L. ZHELUDKEVICH:** Supervision, Conceptualization, Investigation, Formal analysis, Writing − Original draft; **Wei LI:** Sponsorship acquisition, Writing − Review & editing.

Declaration of competing interest

The authors declare that they have no conflicts of interest to this work. We declare that we do not have any commercial or associative interest that represents a conflict of interest in connection with the work submitted.

Data availability

The raw/processed data required to reproduce these findings cannot be shared at this time as the data also forms part of an ongoing study.

Acknowledgments

Jun-jie YANG appreciates the financial support by the National Natural Science Foundation of China (No. 52101084), Guangdong Basic and Applied Basic Research Foundation, China (Nos. 2023A1515011579, 2020A1515110754), and Guangzhou Basic and Applied Basic Research Foundation, China (No. 202102020612).

Supporting Information

Supporting Information associated with this article can be found at http://tnmsc.csu.edu.cn/download/10-p1496-2023-0044-Supporting_Information.pdf.

References

[1] LI Ying-ju, LUO Tian-jiao, YANG Yuan-sheng. Effects of trace element and purification on properties of AZ80 magnesium alloy [J]. Transactions of Nonferrous Metals Society of China, 2010, 20(Suppl.): 407−410.

[2] CHENG Ying-liang, QIN Ting-wei, WANG Hui-min, ZHANG Zhao. Comparison of corrosion behaviors of AZ31, AZ91, AM60 and ZK60 magnesium alloys [J]. Transactions of Nonferrous Metals Society of China, 2009, 19: 517−524.

[3] BAGHNI I M, WU Y S, LI J Q, ZHANG W. Corrosion behavior of magnesium and magnesium alloys [J]. Transactions of Nonferrous Metals Society of China, 2004, 14: 1−10.

[4] ZHOU Peng, YANG Li-xin, HOU Yao-jun, DUAN Guo-qing, YU Bao-xing, LI Xue-jie, ZHAI Yun-fei, ZHANG Bo, ZHANG Tao, WANG Fu-hui. Grain refinement promotes the formation of phosphate conversion coating on Mg alloy AZ91D with high corrosion resistance and low electrical contact resistance [J]. Corrosion Communications, 2021, 1: 47−57.

[5] LI Pu-bo, SHAO Ze-xi, FU Wei, MA Wei, YANG Kun, ZHOU Hai, GAO Mang-mang. Enhancing corrosion resistance of magnesium alloys via combining green chicory extracts and metal cations as organic-inorganic composite inhibitor [J]. Corrosion Communications, 2023, 9: 44−56.

[6] CAIN T, MADDEN S B, BIRBILIS N, SCULLY J R. Evidence of the enrichment of transition metal elements on corroding magnesium surfaces using Rutherford backscattering spectrometry [J]. Journal of the Electrochemical Society, 2015, 162: 228−237.

[7] YANG Lei, LIU Guang-kun, MA Lian-gong, ZHANG Er-lin, ZHOU Xiao-rong, THOMPSON G. Effect of iron content on the corrosion of pure magnesium: Critical factor for iron tolerance limit [J]. Corrosion Science, 2018, 139: 421−429.

[8] SONG G L, ATRENS A. Corrosion mechanisms of magnesium alloys [J]. Advanced Engineering Materials, 1999, 1: 11−33.

[9] MCNULTY R E, HANAWALT J D. Some corrosion characteristics of high purity magnesium alloys [J]. Transactions of the Electrochemical Society, 1942, 81: 423−433.

[10] SIMANJUNTAK S, CAVANAUGH M K, GANDEL D S, EASTON M A, GIBSON M A, BIRBILIS N. The influence of iron, manganese, and zirconium on the corrosion of magnesium: An artificial neural network approach [J]. Corrosion, 2015, 71: 199−208.

[11] SAMANIEGO A, BIRBILIS N, XIA X, FRANKEL G S. Hydrogen evolution during anodic polarization of Mg

alloyed with Li, Ca, or Fe [J]. Corrosion, 2015, 71: 224−233.
[12] TAUB I A, ROBERTS W, LAGAMBINA S, KUSTIN K. Mechanism of dihydrogen formation in the magnesium−water reaction [J]. The Journal of Physical Chemistry A, 2002, 106: 8070−8078.
[13] YANG Lei, ZHOU Xiao-rong, LIANG Song-mao, SCHMID F R, FAN Zong-yun, SCAMANS G, ROBSON J, THOMPSON G. Effect of traces of silicon on the formation of Fe-rich particles in pure magnesium and the corrosion susceptibility of magnesium [J]. Journal of Alloys and Compounds, 2015, 619: 396−400.
[14] WILLIAMS G, BIRBILIS N, MCMURRAY H N. Controlling factors in localised corrosion morphologies observed for magnesium immersed in chloride containing electrolyte [J]. Faraday Discussions, 2015, 180: 313−330.
[15] SALLEH S H, THOMAS S, YUWONO J A, VENKATESAN K, BIRBILIS N. Enhanced hydrogen evolution on $Mg(OH)_2$ covered Mg surfaces [J]. Electrochimica Acta, 2015, 161: 144−152.
[16] FAJARDO S, FRANKEL G S. Effect of impurities on the enhanced catalytic activity for hydrogen evolution in high purity magnesium [J]. Electrochimica Acta, 2015, 165: 255−267.
[17] LYSNE D, THOMAS S, HURLEY M F, BIRBILIS N. On the Fe enrichment during anodic polarization of Mg and its impact on hydrogen evolution [J]. Journal of the Electrochemical Society, 2015, 162: C396−C402.
[18] FRANKEL G S, FAJARDO S, LYNCH B M. Introductory lecture on corrosion chemistry: A focus on anodic hydrogen evolution on Al and Mg [J]. Faraday Discussions, 2015, 180: 11−33.
[19] THOMAS S, MEDHEKAR N V, FRANKEL G S, BIRBILIS N. Corrosion mechanism and hydrogen evolution on Mg [J]. Current Opinion in Solid State and Materials Science, 2015, 19: 85−94.
[20] MITROVIC S V, PACKWOOD R H, CARPENTER G J C, BRIGHAM R J. On the concentration of iron dissolved in magnesium [J]. Canadian Metallurgical Quarterly, 1994, 33: 61−65.
[21] TAHERI M, KISH J R, BIRBILIS N, DANAIE M, MCNALLY E A, MCDERMID J R. Towards a physical description for the origin of enhanced catalytic activity of corroding magnesium surfaces [J]. Electrochimica Acta, 2014, 116: 396−403.
[22] HÖCHE D, BLAWERT C, LAMAKA S V, SCHARNAGL N, MENDIS C, ZHELUDKEVICH M L. The effect of iron re-deposition on the corrosion of impurity-containing magnesium [J]. Phys Chem Chem Phys, 2016, 18: 1279−1291.
[23] YASAKAU K A, HÖCHE D, LAMAKA S L, FERREIRA M G S, ZHELUDKEVICH M L. Kelvin microprobe analytics on iron-enriched corroded magnesium surface [J]. Corrosion, 2017, 73: 583−595.
[24] MERCIER D, SWIATOWSKA J, ZANNA S, SEYEUX A, MARCUS P. Role of segregated iron at grain boundaries on Mg corrosion [J]. Journal of the Electrochemical Society, 2018, 165: C42−C49.
[25] LI J C, SUN W H, HURLEY B, LUO A A, BUCHHEIT R G. Cu redistribution study during the corrosion of AZ91 using a rotating ring-disk collection experiment [J]. Corrosion Science, 2016, 112: 760−764.
[26] ZHANG Yu, GORE P, RONG W, WU Yu-juan, YAN Yuan-ming, ZHANG Rui-feng, PENG Li-ming, NIE Jian-feng, BIRBILIS N. Quasi-in-situ STEM-EDS insight into the role of Ag in the corrosion behaviour of Mg−Gd−Zr alloys [J]. Corrosion Science, 2018, 136: 106−118.
[27] LAMAKA S V, HÖCHE D, PETRAUSKAS R P, BLAWERT C, ZHELUDKEVICH M L. A new concept for corrosion inhibition of magnesium: Suppression of iron re-deposition [J]. Electrochemistry Communications, 2016, 62: 5−8.
[28] LAMAKA S V, VAGHEFINAZARI B, MEI D, PETRAUSKAS R P, HÖCHE D, ZHELUDKEVICH M L. Comprehensive screening of Mg corrosion inhibitors [J]. Corrosion Science, 2017, 128: 224−240.
[29] YANG Jun-jie, BLAWERT C, LAMAKA S V, YASAKAU K A, WANG Li, LAIPPLE D, SCHIEDA M, DI Shi-chun, ZHELUDKEVICH M L. Corrosion inhibition of pure Mg containing a high level of iron impurity in pH neutral NaCl solution [J]. Corrosion Science, 2018, 142: 222−237.
[30] FOCKAERT L I, WÜRGER T, UNBEHAU R, BOELEN B, MEIßNER R H, LAMAKA S V, ZHELUDKEVICH M, TERRYN H, MOL J M C. ATR-FTIR in Kretschmann configuration integrated with electrochemical cell as in situ interfacial sensitive tool to study corrosion inhibitors for magnesium substrates [J]. Electrochimica Acta, 2020, 345: 136166.
[31] YANG Lei, ZHOU Xiao-rong, CURIONI M, PAWAR S, LIU Hong, FAN Zhong-yun, SCAMANS G, THOMPSON G. Corrosion behavior of pure magnesium with low iron content in 3.5 wt% NaCl solution [J]. Journal of the Electrochemical Society, 2015, 162: C362−C368.
[32] SASTRI V S. Green corrosion inhibitors: Theory and practice [M]. New York: John Wiley & Sons, 2012.
[33] MARTELL A E, HANCOCK R D. Metal complexes in aqueous solutions [M]. Heidelberg: Springer, 2013.
[34] SZEWCZYK G, WISNIEWSKI K. Handbook for cleaning/decontamination of surfaces [M]. Amsterdam: Elsevier, 2007: 125−195.
[35] HU S, SHANER M R, BEARDSLEE J A, LICHTERMAN M, BRUNSCHWIG B S, LEWIS N S. Amorphous TiO_2 coatings stabilize Si, GaAs, and GaP photoanodes for efficient water oxidation [J]. Science, 2014, 344: 1005−1009.
[36] FENG Ling, LI Min, LIU Guo-qiang, HAN Lei, YANG Ru. Porous structure and adsorption properties of magnesium trisilicate synthesized by a precipitation method [J]. Journal of Beijing University of Chemical Technology (Natural Science Edition), 2010, 37: 70−76. (in Chinese)
[37] KOVAČEVIĆ N, KOKALJ A. The relation between adsorption bonding and corrosion inhibition of azole molecules on copper [J]. Corrosion Science, 2013, 73: 7−17.
[38] LI Xiang-hong, XIE Xiao-guang, DENG Shu-duan, DU Guan-ben. Inhibition effect of two mercaptopyrimidine derivatives on cold rolled steel in HCl solution [J]. Corrosion Science, 2015, 92: 136−147.
[39] ABDALLAH M, HELAL E A, FOUDA A S. Aminopyrimidine derivatives as inhibitors for corrosion of 1018 carbon steel in nitric acid solution [J]. Corrosion Science, 2006, 48: 1639−1654.

[40] TIAN H, LI W, CAO K, HOU B. Potent inhibition of copper corrosion in neutral chloride media by novel non-toxic thiadiazole derivatives [J]. Corrosion Science, 2013, 73: 281−291.
[41] JU Hong, KAI Zhen-Peng, LI Yan. Aminic nitrogen-bearing polydentate Schiff base compounds as corrosion inhibitors for iron in acidic media: A quantum chemical calculation [J]. Corrosion Science, 2008, 50: 865−871.
[42] WÜRGER T, FEILER C, MUSIL F, FELDBAUER G B V, HÖCHE D, LAMAKA S V, ZHELUDKEVICH M L, MEIßNER R H. Data science based Mg corrosion engineering [J]. Frontiers in Materials, 2019, 6: 1−9.
[43] FEILER C, MEI D, VAGHEFINAZARI B, WÜRGER T, MEIßNER R H, LUTHRINGER-FEYERABEND B J C, WINKLER D A, ZHELUDKEVICH M L, LAMAKA S V. In silico screening of modulators of magnesium dissolution [J]. Corrosion Science, 2020, 163: 108245.
[44] LAMAKA S V, GONZALEZ J, MEI D, FEYERABEND F, WILLUMEIT R R, ZHELUDKEVICH M L. Local pH and its evolution near Mg alloy surfaces exposed to simulated body fluids [J]. Advanced Materials Interfaces, 2018, 5: 1800169.
[45] WANG C, XU W, HÖCHE D, ZHELUDKEVICH M L, LAMAKA S V. Exploring the contribution of oxygen reduction reaction to Mg corrosion by modeling assisted local analysis [J]. Journal of Magnesium and Alloys, 2023, 11: 100−109.

铁配合型镁合金缓蚀剂的阴极阻蚀机制

杨俊杰[1,2]，王霖倩[3]，Carsten BLAWERT[3], Sviatlana V. LAMAKA[3],
Christian FEILER[3], Mikhail L. ZHELUDKEVICH[3,4]，李 卫[1]

1. 暨南大学 先进耐磨蚀及功能材料研究院，广州 510632；
2. 暨南大学 韶关研究院，韶关 512027；
3. Institute of Surface Science, Helmholtz-Zentrum Hereon (Hereon), 21502 Geesthacht, Germany；
4. Faculty of Engineering, University of Kiel, Kaiserstraße 2, 24143 Kiel, Germany

摘 要：研究阴极缓蚀剂(3-甲基水杨酸盐，3-MeSA)对含铁纯镁腐蚀性能的影响。高铁杂质颗粒成分、腐蚀表面形貌以及 3-MeSA 分子结构特征为揭示含铁镁合金的腐蚀行为及 3-MeSA 的阴极型阻蚀机理提供了实验与理论依据。研究结果表明：含铁杂质颗粒中含有固溶态硅，而 Fe/Si 比可能是导致不同局部腐蚀形态差异的主要原因。虽然 3-MeSA 能在镁基体上形成吸附层，但其阻蚀机制主要归因于其螯合从富铁颗粒中自腐蚀释放 Fe^{2+}/Fe^{3+}的能力，阻止被还原的铁物质再次沉积至腐蚀金属表面。

关键词：镁；富铁杂质；铁配合剂；阴极型缓蚀剂；量子化学计算

(Edited by Wei-ping CHEN)